IEEE Access
Multidisciplinary ⋮ Rapid Review ⋮ Open Access Journal

Received March 9, 2020, accepted March 18, 2020, date of publication March 23, 2020, date of current version April 7, 2020.

Digital Object Identifier 10.1109/ACCESS.2020.2982740

Trajectory Planning With Lamé-Curve Blending for Motor-Saturation Avoidance Upon Mobile-Robot Turning

XING WU[1,2], JORGE ANGELES[2], (Life Fellow, IEEE), TING ZOU[3], JUNJIE YANG[1], HONGKAI LI[1], AND WEI LI[4]

[1]College of Mechanical and Electrical Engineering, Nanjing University of Aeronautics and Astronautics, Nanjing 210016, China
[2]Centre for Intelligent Machines, McGilll University, Montreal, QC H3A 0C3, Canada
[3]Department of Mechanical Engineering, Memorial University of Newfoundland, St. John's, NL A1B 3X5, Canada
[4]State Key Laboratory of Mechanical System and Vibration, Shanghai Jiao Tong University, Shanghai 200240, China

Corresponding author: Xing Wu (wustar5353@nuaa.edu.cn)

This work was supported in part by the National Natural Science Foundation of China under Grant 61973154, in part by the Natural Sciences and Engineering Research Council of Canada under Grant 4532-2010, in part by the National Defense Basic Scientific Research Program of China under Grant JCKY2018605C004, and in part by the Fundamental Research Funds for the Central Universities of China under Grant NS2019033.

ABSTRACT In order to avoid motor saturation in turning maneuvers, an iterative Lamé-trajectory planning scheme is proposed to generate a smooth curvature-bounded transition trajectory for a differential-driving wheeled mobile robot (DWMR) switching from one straight path to another. The scheme consists of Lamé-curve blending, inverse-kinematics computation, peak-torque positioning and torque-saturation avoidance. Firstly, a Lamé-curve blending procedure based on affine transformations, is formulated to generate a smooth G^2-continuous transition trajectory for connecting two straight paths. Secondly, the platform twist is calculated according to the curvature of the Lamé-curve trajectory, then transformed into the actuated-joint rates by means of the inverse-kinematics model. Thirdly, a peak-torque positioning technique is developed to estimate the peak torques of the driving wheels when the DWMR tracks the trajectory, by combining the computed-torque method and the inverse-dynamics model. Finally, an iterative r-step saturation-avoidance prediction planning strategy is devised to suppress the peak motor torques, by means of two torque limitation schemes via adjusting trajectory curvature and robot speed. The simulation results show that, compared with the conventional planning techniques for circular arcs, our trajectory planning scheme can generate a smooth saturation-free transition trajectory with feasible curvature and traveling speed. The scheme is significantly beneficial for trajectory tracking under finite actuation torque in turning maneuvers, thereby preventing any possible path deviation caused by insufficient torque.

INDEX TERMS Mobile robot, trajectory planning, curve blending, torque computation, motor saturation.

I. INTRODUCTION

Automated guided vehicles (AGVs) have been typical industrial mobile robots, used for repeated transportation tasks in factories for decades [1]–[3]. Guidance, navigation and control (GNC) are essential factors in mobile robots [4]. Guidance involves defining a trajectory for a mobile robot from its position and orientation in order to follow a given path. Given paths, also termed guide paths, the target to be followed by the robot, can be generated in various possible ways: path planning in a map (environment model) [5]–[8]; a virtual reference in a fixed coordinate frame [9]–[11]; and a physical landmark (wire, tape, stripe) on the ground [12]–[14].

In order to have a mobile robot follow the target trajectory planned by the guidance system, trajectory tracking techniques can be used for real-time motion control. The controller design mainly falls into two categories: simple controller based only on the kinematics model; and integration of the former via robot dynamics. Kinematics models usually lead to velocity-driven, first-order differential equations [2], [5], [11], [12]. Sometimes these models are turned into geometric equations based on the instantaneous centre

The associate editor coordinating the review of this manuscript and approving it for publication was Hassen Ouakad.

of curvature or trajectory approximation at each sampling instant [7], [15]. As pointed out by Fierro and Lewis [16], the kinematic controller can simplify the nonholonomic tracking problem. However, the actual *twist*[1] is generated based on the assumption of ''perfect twist tracking'', which does not hold in reality.

Formulation of the nonholonomic controller at the dynamics level makes it realistic and practical for industrial applications. Dynamics models are normally force-driven, second-order differential equations relating wheel forces to robot acceleration [9], [12]. When motor dynamics is included, dynamics models evolve to composite models. In these models, the platform twist can be associated with the time-derivative of motor-armature voltage [10], or with the duty ratio of pulse-width modulation (PWM) of motor voltage [17], or even with the motor current [18].

Generally speaking, mobile robots only need to consume low actuation power in constant-speed straight motion. However, the peak actuation torque is required for curvilinear maneuver with fast variation of speed and direction [19]–[21]. For example, the control torque has a high peak value and a series of sharp fluctuations in the transient state when a robot tracks a step reference trajectory [19], or when a robot tracks a circular reference trajectory with large initial position and/or orientation deviations [21]. It is known that the peak torque needed in sharp curvilinear maneuvers may exceed dozens of times, or even hundreds of times, the torque in steady-state straight motion. Actuator saturation tends to happen in the presence of agile maneuvers.

Essentially, actuator saturation is caused by the constraints on electrical actuation capacity, in the presence of highly demanding robot maneuvers. Typical constraint factors include: battery voltage constraint on the duty ratio of PWM for motors [17]; battery voltage constraint on a curvature-bounded smooth path [22]; actuator-velocity saturation restricting the decoupling between translation and rotation of an omnidirectional MR [23]; minimum-jerk velocity-planning for a parametric path [24]; and a torque-bounded controller based on one-step-ahead backstepping [25]. Besides, actuator saturation is possible to occur in any practical system, as the amplitude and the operating rate of actuators are limited by environment and machine structure [26].

In the literature, the actuator-saturation avoidance schemes for mobile robots can mainly be classified into two categories: torque-bounded controller design and curvature-bounded trajectory planning. For the former category, a new virtual control law, which is a function of both state variables, was designed by Do [25]. Consequently, the magnitude of the control input can be bounded by an arbitrarily small positive constant by choosing appropriate controller constants. Xu [20] proposed a nonlinear robust control algorithm that was chatter-free, saturation-avoidance with asymptotic stability. For the latter category, under bounded control inputs due to the battery voltage, the curvature-bounded path based on a smooth clothoid curve was generated for the translational motion of mobile robots [22]. The trajectory planning problem for a differential-driving wheeled mobile robot (DWMR) traversing a crank-shaped path with two corners was converted into a process of duration-time planning of PWM inputs [17].

Other than the two approaches mentioned above, Wu *et al.* proposed a towing-mechanism design method to prevent the actuator-saturation problem [12]. A rotational degree of freedom between the tractor and the vehicle allowed the tractor to follow the guide paths rapidly. It is noteworthy that the actual torques of the driving wheels did not show much difference, no matter what kind of paths, straight or curvilinear, the robotic vehicle tracked, as shown in Fig.14 in the foregoing reference. This is totally different from the variation process of motor torque needed by conventional DWMRs, as described in the literature [19]–[21]. However, this rotational degree of freedom also results in the difficulty of controlling the pose of the robotic vehicle precisely on the guide path.

As the causes of actuator saturation are not always known or predictable, such as external disturbance, model nonlinearity and parameters uncertainties, many constrained control strategies have been used to cope with these factors robustly [20], [25], [26]. However, if we already know that target trajectory is the dominant factor that leads to actuator saturation, curvature-bounded trajectory planning will be the most pertinent method to avoid saturation effectively [17], [22]. The problem addressed in this paper is oriented to motor-saturation avoidance in turning maneuvers. Therein, the shape and curvature of the transition trajectory influence the robot motion directly. Thus, the focus of the paper is mainly the trajectory planning scheme, without explicit consideration of disturbance factors.

It is noteworthy that when a smooth saturation-free transition trajectory with feasible curvature is given to a robot, it is significantly beneficial for trajectory tracking controllers, including the pure kinematics controller, since the computed motor torques do not exceed the rated value theoretically. The underlying motivation behind this paper lies in developing a curvature-bounded, saturation-avoidance trajectory planning scheme for guidance control of a DWMR in turning maneuvers between two straight paths. Needless to say, our research work pertains to the second category of actuator-saturation avoidance schemes. The main contribution of this paper is threefold:

(1) A novel straight line-Lamé curve-straight line (SCS) path generation procedure based on affine transformations is proposed for the guidance control of a robot upon turning maneuvers. Compared with the clothoid curve used for connecting two straight lines [22], the Lamé curve can provide the full trajectory with G^2-continuity, especially smooth bounded curvature, which is inclined to only need moderate torque outputs in trajectory tracking.

[1]The rigid-body twist is a vector array that includes point velocity and angular velocity.

(2) A peak-torque positioning technique is devised by combining the computed-torque method with the dynamics model. Rather than determining the time-optimality condition relating robot acceleration to battery voltage inputs [22], torque limits are directly adopted as a benchmark in our technique. Hence, the actuation torque needed by the DWMR at any point can be readily computed based on the dynamics model; then, motor saturation will be efficiently detected in advance.

(3) An iterative r-step saturation-avoidance prediction planning strategy is developed based on two torque limitation schemes: adjusting trajectory curvature and robot speed. Two different objectives for guidance control, motor saturation and time efficiency, are taken into account. Instead of constructing a set of optimal voltage input vectors, as done by Kim and Kim [22], a smooth Lamé curve with feasible curvature is provided by our strategy as the transition trajectory, free of motor saturation in the ensuing control cycles. Common trajectory tracking techniques [9], [10], [21], [27], [28] can be integrated with our scheme seamlessly.

The balance of the paper is organized as follows: problem description and methodology overview are provided in Section II; the SCS path generation procedure is formulated in Section III; the motor-torque computation technique is investigated in Section IV; the iterative r-step saturation-avoidance prediction planning strategy is developed in Section V; simulation results with data analysis are reported in Section VI, while conclusions and recommendations for future research work are included in Section VII.

II. PROBLEM FORMULATION

A. SCS PATH PLANNING

The problem under study lies in planning a smooth transition trajectory to prevent motor saturation, in the presence of turning maneuvers from one straight path to another. The platform of the DWMR is depicted as a triangle-shaped rigid body in Fig. 1.

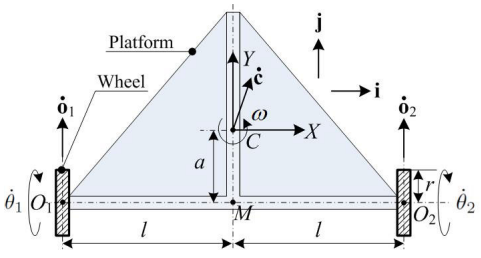

FIGURE 1. Diagram of a DWMR.

Two coaxial wheels are coupled to the platform by means of revolutes of axes passing through points O_1 and O_2. Let C be the centre of mass of the platform. Point M is the midpoint of segment $\overline{O_1\ O_2}$. Moreover, the position vectors of C, O_1 and O_2 in an inertial frame are denoted by $\mathbf{c}$, $\mathbf{o}_1$ and $\mathbf{o}_2$, respectively. Additionally, let ω be the scalar angular velocity of the platform about a vertical axis. In order to proceed with the kinematics analysis of this system, we define a moving frame $\mathcal{F}$, of axes X, Y, Z, attached to the platform, with Z pointing in the upward vertical direction. Unit vectors $\mathbf{i}$, $\mathbf{j}$, $\mathbf{k}$ are defined parallel to axes X, Y, Z, respectively.

As shown in Fig. 2(a), two straight paths, path 1 and path 2, intersect at point M_k, making an angle $\angle CM_kT_k = 2\psi$. The DWMR is moving along path 1, then switching to path 2. Point C is used as a reference point on the robot chassis, indicating its position on a path or trajectory. Point T_k is the first point that the robot tracks when it enters path 2. If the transition trajectory is symmetric as assumed henceforth, then $\overline{CM_k} = \overline{M_kT_k}$. In this case, the position of point T_k on path 2 is determined by that of point C on path 1.

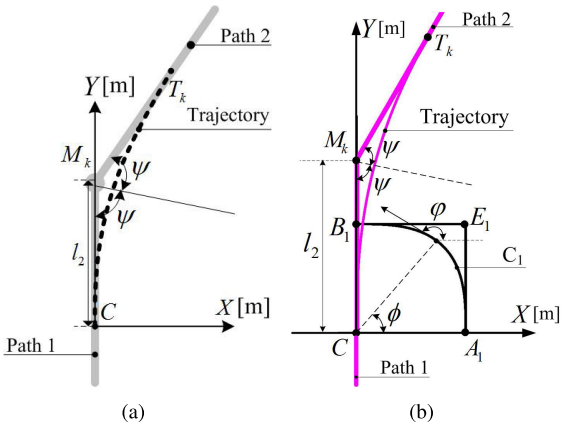

FIGURE 2. Turning maneuver between two straight paths: (a) SCS path; (b) Curve blending.

Several turning maneuvers are optional for the DWMR to change its path. One simple way is to stop at the intersection point M_k, then turning about it in order to orientate the robot according to path 2. Apparently, this way requires to interrupt the continuous movement of the DWMR, thereby decreasing the turning efficiency significantly.

For non-stop turning maneuvers, it is necessary to plan a curvilinear transition trajectory connecting two straight paths. A group of paths, consisting of a first straight line, a curve and a second straight line, are merged into one single turning path at the connecting points, which we term a SCS path. Several types of curves can be used here to blend two straight paths. Compared with circular arcs and clothoid curves, *Lamé* curves can provide the full trajectory with G^2-continuity, meaning that position, tangent and curvature are all continuous along the full trajectory, including the blending points [29].

As shown in Fig. 2(b), the transition trajectory, on which a robot moves from path 1 toward path 2, can be obtained by curve transformation. C_1 is a standard Lamé curve, intersecting the X- and Y-axes at points A_1 and B_1, respectively. The difference of the orientation angle at these two points is a right angle, $\angle A_1\ E_1\ B_1$, formed by their tangent lines at point E_1. Affine transformations are used to convert Lamé curve C_1

into the transition trajectory, by mapping points B_1, E_1 and A_1 into points C, M_k and T_k, respectively. Consequently, path 1, the smooth transition curve, and path 2 are combined at the blending points C and T_k, thereby generating a SCS turning path.

Essentially, the shape of transition trajectories is determined by the positions of points C and T_k on paths 1 and 2 when affine transformations are used. It is noteworthy that point C, indicating the robot position, moves along path 1. This means that a set of transition trajectories can be obtained in terms of the time-varying positions of the DWMR on path 1. Since these trajectories are all smooth, with G^2-continuity, the motor torques needed by the robot to track the trajectories are, consequently, smooth and continuous. However, trajectories with different shapes will have different peak curvature distributions, thereby influencing the peak torques of a robot travelling on different transition trajectories. In order to verify whether the peak torques exceed the rated torque, the planned trajectories should be integrated with the computed -torque method based on the inverse-dynamics model. Therein, a methodology overview, based on both the kinematics and dynamics models of the robot, is required.

B. METHODOLOGY OVERVIEW

In order to avoid motor saturation in turning maneuvers from one straight path to another, an iterative Lamé-trajectory planning scheme is proposed for mobile robots. The methodology overview for the guidance control architecture is illustrated in Fig. 3. Electric motors, the actuators of choice in most mobile robots, are assumed in the paper. A typical motor servo control system includes a feedback subsystem with three cascaded loops, i.e., the outer position loop, the intermediate velocity loop and the inner current/torque loop. Nowadays, many commercial off-the-shelf motor drives provide the complete control capability for all three loops. Thus, the motor drives can carry out the control instructions on speed and torque, generated by kinematics or dynamics controllers, as shown in Fig. 3.

In the guidance control architecture, the trajectory planning scheme is integrated with the tracking control method to maneuver a mobile robot by means of motors and their drives. A target trajectory is provided by the planning scheme to the tracking controller, either kinematics or dynamics. The former generates the joint-rates command to the motor drives, while the latter produces the torque command to them. When the mobile robot is actuated to move in the environment, the external disturbances, as well as the model nonlinearity and parameter uncertainty, will deteriorate its motion accuracy and stability. Hence, a number of constrained control strategies have been used to cope with these disturbance factors robustly [20], [25], [26].

However, it is noteworthy that trajectory tracking control is outside of the scope of our paper. As mentioned above, the theme of our paper is oriented to the dominant factor of motor saturation in turning maneuvers. The key point lies in the generation of a smooth saturation-free transition trajectory for two straight paths. The trajectory planning scheme consists of Lamé-curve blending, inverse-kinematics computation, peak-torque positioning and torque-saturation avoidance, as highlighted in the golden dotted-line block in Fig. 3.

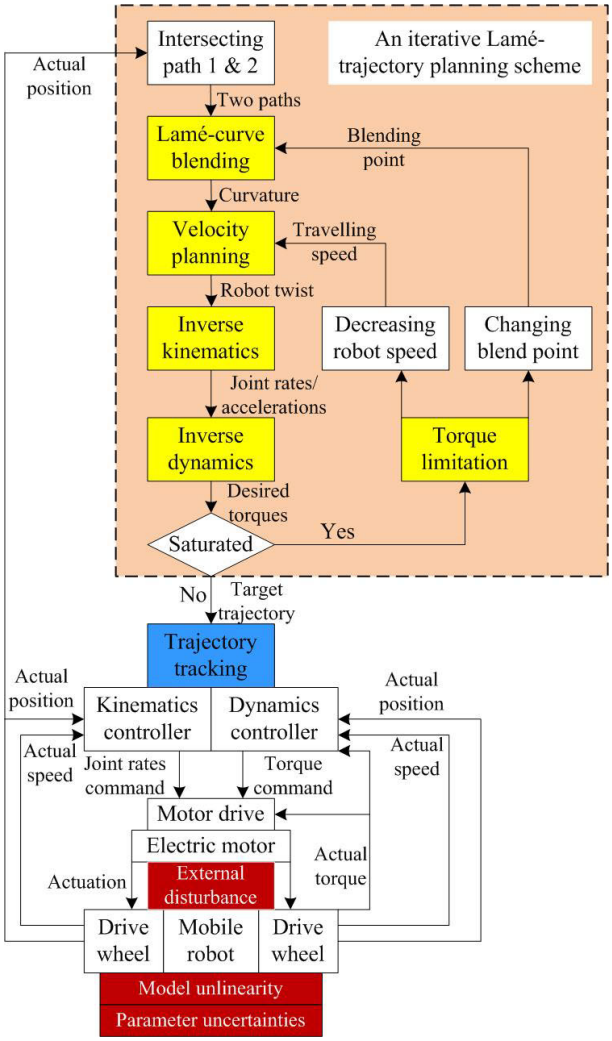

FIGURE 3. Guidance control methodology.

According to the two straight paths, detected by a localization system, a Lamé-curve blending procedure, based on affine transformations is formulated to generate a smooth G^2-continuous transition trajectory, as the first-layer output. Then, when the robot tracks the transition trajectory at a given speed, the robot twist, as the second-layer output, will be influenced by the curvature of the transition trajectory. Moreover, the inverse-kinematics model can transform the twist into the actuated joint-rate vector, as the third-layer output. Furthermore, the desired torque is calculated based on the inverse-dynamics model for the motor drives, as the fourth-layer output. If the desired torque is higher than the rated torque, the motor will be saturated. In order to avoid motor saturation, an iterative r-step prediction planning strategy is devised to suppress the peak motor torques, by means

of two torque limitation schemes via adjusting blending point and decreasing robot speed.

It is noteworthy that the trajectory planning scheme is implemented online iteratively. This means that before the robot approaches the intersection of the two straight paths, the iterative planning scheme has been already used to predict the trajectory curvature and motor torques. This is done for each upcoming initial point of curve blending in turning maneuvers. Hence, the scheme can help the robot determine the appropriate moment or adjust the feasible speed in advance before it starts the turning maneuver.

III. SCS PATH GENERATION

A. LAMÉ-CURVE BLENDING

The cubic Lamé curve, the lowest order of this curve family with a variable curvature, is chosen as the transition trajectory for turning maneuvers. This curve is defined as [29]

$$\left(\frac{x}{g_x}\right)^3 + \left(\frac{y}{g_y}\right)^3 = 1 \tag{1}$$

where $0 \le x \le g_x, 0 \le y \le g_y$, while g_x and g_y denote one-half the side lengths of the circumscribing rectangle. In this case, we use a symmetric Lamé curve, which means $g_x = g_y$.

As shown in Fig. 2(b), the orientation angle of an arbitrary point on the standard Lamé curve C_1 is defined as the angle ϕ that the position vector of the point makes with the X-axis. The explicit parametric equations of this curve can be expressed in terms of the parameter ϕ $(0 \le \phi < \pi/2)$ as

$$x(\phi) = \frac{g_x}{(1+\tan^3\phi)^{1/3}}, \quad y(\phi) = \frac{g_y \tan\phi}{(1+\tan^3\phi)^{1/3}} \tag{2}$$

Lamé curve C_1 in Fig. 4 is defined as in Eq. (2). In order to blend two straight lines on a SCS path, affine transformations are exerted on Lamé curve C_1 to both conform its shape and change its location in frame $\mathcal{F}$. These operations result in a set of new offspring Lamé curves C_j, with blending points A_j and B_j, and intersection point E_j, where $j = 2, 3, 4$. Finally, a smooth transition trajectory is generated, tangent to paths 1 and 2 at points C and T_k, the tangent lines intersecting at point M_k.

The homogeneous coordinates of Lamé curve C_j $(j = 1, 2, 3, 4)$ and of the transition trajectory are stored in arrays $\mathbf{p}_j$ $(j = 1, 2, 3, 4)$ and $\mathbf{p}_5$. The rotation, scaling and displacement matrices are $\mathbf{R}(\varphi)$, $\mathbf{S}(s_x, s_y)$ and $\mathbf{D}$, where φ is defined in Fig. 2(b), s_x and s_y being the scaling factors along the X- and Y-axes. The first two matrices are given below, while the third matrix will be obtained as a product of affine transformations.

$$\mathbf{R}(\varphi) \equiv \begin{bmatrix} \cos\varphi & -\sin\varphi & 0 \\ \sin\varphi & \cos\varphi & 0 \\ 0 & 0 & 1 \end{bmatrix} \tag{3}$$

$$\mathbf{S}(s_x, s_y) \equiv \begin{bmatrix} S_x & 0 & 0 \\ 0 & S_y & 0 \\ 0 & 0 & 1 \end{bmatrix} \tag{4}$$

The position vectors of an arbitrary point on the parametric equations of the Lamé curves C_j $(j = 1, 2, 3, 4)$ are denoted as $\mathbf{p}_j$. The homogeneous coordinates of points B_j, E_j, A_j, C, M_k and T_k are stored in arrays $\mathbf{b}_j$, $\mathbf{e}_j$, $\mathbf{a}_j$, $\mathbf{c}_k$, $\mathbf{m}_k$ and $\mathbf{t}_k$, respectively. Moreover, five homogeneous coordinate matrices: $\mathbf{N}_j = [\mathbf{b}_j\ \mathbf{e}_j\ \mathbf{a}_j]$ $(j = 1, 2, 3, 4)$, and $\mathbf{N}_5 = [\mathbf{c}_k\ \mathbf{m}_k\ \mathbf{t}_k]$, are defined. Among them, vector blocks are all three dimensional—their entries are the homogeneous coordinates of the corresponding points in the planar frame $\mathcal{F}$. Matrices $\mathbf{N}_1$ and $\mathbf{N}_5$ can be obtained from the homogeneous coordinates of the starting points B_1, E_1 and A_1 on curve C_1, and of the desired points C, M_k and T_k on the final transition trajectory, namely,

$$\mathbf{N}_1 = \begin{bmatrix} 0 & 1 & 1 \\ 1 & 1 & 0 \\ 1 & 1 & 1 \end{bmatrix}, \quad \mathbf{N}_5 = \begin{bmatrix} 0 & 0 & l_2 \sin 2\psi \\ 0 & l_2 & l_2(1-\cos 2\psi) \\ 1 & 1 & 1 \end{bmatrix} \tag{5}$$

The corresponding affine transformations follow:

Step 1: Rotate Lamé curve C_1 through $\pi/4$ about point C counterclockwise to obtain Lamé curve C_2. Hence, the parametric equation of Lamé curve C_2 can be obtained by using a rotation transformation, Eq. (3), from that of curve C_1, i.e., $\mathbf{p}_2 = \mathbf{R}(\pi/4)\mathbf{p}_1$.

Step 2: Conform Lamé curve C_2 to curve C_3 in order to make the difference of the orientation angles $\angle A_3\, E_3\, B_3 = 2\psi$. Since $y_3 = y_2$ and $x_3 = x_2 \tan\psi$, as shown in Fig. 4, the parametric equation of Lamé curve C_3 can be obtained by using a scaling transformation, Eq. (4), from that of curve C_2, i.e., $\mathbf{p}_3 = \mathbf{S}(\tan\psi, 1)\mathbf{p}_2$.

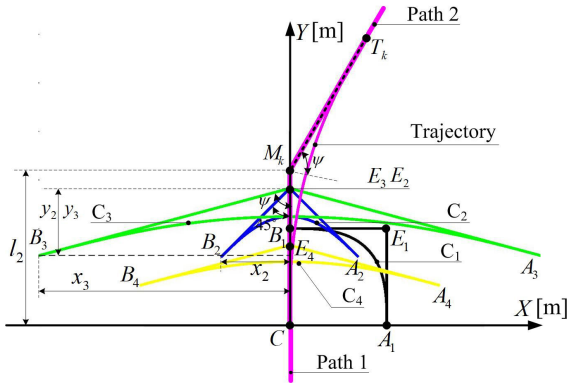

FIGURE 4. Affine transformations of Lamé curves for SCS path.

Step 3: Isotropically scale[2] Lamé curve C_3 to curve C_4 according to the distance l_2. Let the scaling factor be k_1, and the length of segment $\overline{B_3\, E_3}$ be l_1, where $k_1 = l_2/l_1$. Hence, the parametric equation of Lamé curve C_4 can be obtained by using a isotropically scaling transformation, Eq. (4), from that of curve C_3, i.e., $\mathbf{p}_4 = \mathbf{S}(k_1, k_1)\mathbf{p}_3$. It is noteworthy that isotropic scaling changes the size of Lamé curve C_3 but

[2]An isotropic planar scaling is a resizing of a planar figure by means of identical scalar factors in two orthogonal directions.

preserves its shape. In this step, Lamé curve C_4 has the size and shape required by the final transition trajectory.

Step 4: Displace Lamé curve C_4 to the final transition trajectory, making points B_4, E_4 and A_4 coincide with points C, M_k and T_k, respectively. Find a homogeneous displacement matrix $\mathbf{D}$ satisfying $\mathbf{N}_5 = \mathbf{D}\mathbf{N}_4$.

In order to simplify the calculation, steps 3 and 4 are combined to obtain the homogeneous coordinates of the transition trajectory from Lamé curve C_3 directly [30], i.e.,

$$\mathbf{p}_5 = \mathbf{N}_5\mathbf{N}_3^{-1}\mathbf{S}(\tan\psi, 1)\mathbf{R}(\pi/4)\mathbf{p}_1 \tag{6}$$

with matrix $\mathbf{N}_3$ given by

$$\mathbf{N}_3 = \mathbf{S}(\tan\psi, 1)\mathbf{R}(\pi/4)\mathbf{N}_1 \tag{7}$$

According to Eqs. (5)–(7), the composite affine transformation matrix is calculated as

$$\mathbf{T}_5 \equiv \mathbf{N}_5\mathbf{N}_3^{-1}\mathbf{S}(\tan\psi, 1)\mathbf{R}(\pi/4) = \begin{bmatrix} 0 & -l_3 & l_3 \\ l_2 & l_4 & -l_4 \\ 0 & 0 & 1 \end{bmatrix} \tag{8}$$

with l_3 and l_4 defined as

$$l_3 = l_2 \sin 2\psi, \quad l_4 = l_2 \cos 2\psi \tag{9}$$

B. ROBOT KINEMATICS

As shown in Fig. 1, the radius of the driving wheels is r, the distance between the wheels being $2l$. Let the distance between C and M be a. The scalar angular velocity ω of the platform can be obtained in terms of the angular rates of the driving wheels, $\dot\theta_1$ and $\dot\theta_2$, namely,

$$\omega = \frac{r}{2l}(\dot\theta_2 - \dot\theta_1) \tag{10}$$

Similarly, the velocity $\dot{\mathbf{c}}$ of point C can also be expressed in terms of $\dot\theta_1$ and $\dot\theta_2$, according to the robot kinematics [31].

$$\dot{\mathbf{c}} = \frac{ar}{2l}(\dot\theta_1 - \dot\theta_2)\mathbf{i} + \frac{r}{2}(\dot\theta_1 + \dot\theta_2)\mathbf{j} \tag{11}$$

Moreover, the *planar twist* $\mathbf{t}$ of the platform and the two-dimensional vector $\dot{\boldsymbol\theta}$ of actuated joint rates are defined as

$$\mathbf{t} \equiv \begin{bmatrix} \omega \\ \dot{\mathbf{c}} \end{bmatrix} \in \mathbb{R}^3, \quad \dot{\boldsymbol\theta} \equiv \begin{bmatrix} \dot\theta_1 \\ \dot\theta_2 \end{bmatrix} \in \mathbb{R}^2$$

the forward kinematics model of the platform then being expressed as

$$\mathbf{t} = \mathbf{T}\dot{\boldsymbol\theta} \tag{12}$$

with the 3×2 matrix $\mathbf{T}$ defined as

$$\mathbf{T} \equiv \begin{bmatrix} -r/(2l) & r/(2l) \\ (ar/2l)\mathbf{i} + (r/2)\mathbf{j} & -(ar/2l)\mathbf{i} + (r/2)\mathbf{j} \end{bmatrix}$$

Furthermore, the inverse kinematics model of the platform can also be readily calculated based on Eq. (11):

$$\dot{\boldsymbol\theta} = \mathbf{C}^{-1}\dot{\mathbf{c}} \tag{13}$$

with $\mathbf{C}^{-1}$ given by

$$\mathbf{C}^{-1} = \begin{bmatrix} ((l/ar)\mathbf{i} + (1/r)\mathbf{j})^T \\ (-(l/ar)\mathbf{i} + (1/r)\mathbf{j})^T \end{bmatrix} \tag{14}$$

Consequently, the scalar equations of the inverse kinematics model can be expressed as

$$\dot\theta_1 = \frac{v_c}{r} - \frac{l}{r}\omega, \quad \dot\theta_2 = \frac{v_c}{r} + \frac{l}{r}\omega \tag{15}$$

where the longitudinal speed is $v_c \equiv \dot{\mathbf{c}}^T\mathbf{j}$, the speed of the centre of mass.

C. VELOCITY PLANNING

Let the curvature of the Lamé curve Cj and of the trajectory be κ_j and κ_5, respectively. When the DWMR moves along the transition trajectory at a speed v_c, the robot twist is constrained by

$$\omega = -\kappa_5 v_c \tag{16}$$

The curvature of an arbitrary planar curve defined in parametric form is formulated as a function of the derivatives of a point coordinates with respect to the given parameter [32], namely,

$$\kappa = \frac{x'y'' - y'x''}{((x')^2 + (y')^2)^{3/2}} \tag{17}$$

with primes indicating differentiation with respect to the given parameter.

Upon substitution of Eqs. (2) into Eq. (8), one obtains

$$\begin{aligned} x_5 &= \frac{-l_3 t_\phi}{(1 + t_\phi^3)^{1/3}} + l_3 \\ y_5 &= \frac{l_2}{(1 + t_\phi^3)^{1/3}} + \frac{l_4 t_\phi}{(1 + t_\phi^3)^{1/3}} - l_4 \end{aligned} \tag{18}$$

with t_ϕ defined as $t_\phi \equiv \tan\phi$.

Moreover, the first and second derivatives of x_5 and y_5 with respect to the parameter t_ϕ are

$$\begin{aligned} x_5' &= \frac{-l_3}{(1 + t_\phi^3)^{4/3}}, \quad x_5'' = \frac{4l_3 t_\phi^2}{(1 + t_\phi^3)^{7/3}} \\ y_5' &= -\frac{l_2 t_\phi^2 - l_4}{(1 + t_\phi^3)^{4/3}}, \quad y_5'' = \frac{2l_2 t_\phi^4 - 4l_4 t_\phi^2 - 2l_2 t_\phi}{(1 + t_\phi^3)^{7/3}} \end{aligned} \tag{19}$$

Substitution of Eqs. (19) into Eq. (17) yields

$$\kappa_5 = \frac{2l_2 l_3 t_\phi (1 + t_\phi^3)^{4/3}}{(l_3^2 + (l_2 t_\phi^2 - l_4)^2)^{3/2}} \tag{20}$$

The derivative κ_5' of the curvature with respect to t_ϕ is, in turn,

$$\kappa_5' = \frac{k_2(-l_2^2 t_\phi^4(t_\phi^3+5) - 4l_2 l_4 t_\phi^2(t_\phi^3-1) + (l_3^2+l_4^2)(1+5t_\phi^3))}{(l_3^2 + (l_2 t_\phi^2 - l_4)^2)^{5/2}} \tag{21}$$

with k_2 defined as

$$k_2 \equiv 2l_2 l_3 (1 + t_\phi^3)^{1/3} \tag{22}$$

Upon substitution of Eqs. (9) into Eqs. (20) and (21), one readily obtains

$$\kappa_5 = \frac{2\sin(2\psi)t_\phi(1+t_\phi^3)^{4/3}}{l_2(t_\phi^4 - 2\cos(2\psi)t_\phi^2+1)^{3/2}} \tag{23}$$

$$\kappa_5' = \frac{2k_3\sin(2\psi)(1+t_\phi^3)^{1/3}}{l_2(t_\phi^4 - 2\cos(2\psi)t_\phi^2+1)^{5/2}} \tag{24}$$

with k_3 given by

$$k_3 \equiv -t_\phi^4(t_\phi^3+5) - 4\cos(2\psi)t_\phi^2(t_\phi^3-1) + 5t_\phi^3 + 1 \tag{25}$$

Based on Eqs. (15) and (16), when the DWMR moves along the transition trajectory, the actuated joint rates follow in terms of κ_5:

$$\dot\theta_1 = \frac{v_c}{r}(1+l\kappa_5), \quad \dot\theta_2 = \frac{v_c}{r}(1-l\kappa_5) \tag{26}$$

If the DWMR tracks the transition trajectory at a time-varying speed $v_c(t)$, the time-derivatives of the actuated joint rates are

$$\ddot\theta_1 = \frac{\dot v_c}{r}(1+l\kappa_5) + \frac{v_c}{r}l\dot\kappa_5, \quad \ddot\theta_2 = \frac{\dot v_c}{r}(1-l\kappa_5) - \frac{v_c}{r}l\dot\kappa_5 \tag{27}$$

the time-derivative of the curvature being

$$\dot\kappa_5 = \kappa_5'\dot t_\phi \tag{28}$$

Furthermore, we introduce $\dot\theta_a$, $\dot\theta_b$, $\ddot\theta_a$ and $\ddot\theta_b$, defined as

$$\begin{aligned} \dot\theta_a &= \frac{v_c}{r}, \quad \dot\theta_b = \frac{l}{r}v_c\kappa_5 \\ \ddot\theta_a &= \frac{\dot v_c}{r}, \quad \ddot\theta_b = \frac{l}{r}(\dot v_c\kappa_5 + v_c\dot\kappa_5) \end{aligned} \tag{29}$$

Thus, the actuated joint rates and their time-derivatives can be expressed as

$$\begin{aligned} \dot\theta_1 &= \dot\theta_a + \dot\theta_b, \quad \dot\theta_2 = \dot\theta_a - \dot\theta_b \\ \ddot\theta_1 &= \ddot\theta_a + \ddot\theta_b, \quad \ddot\theta_2 = \ddot\theta_a - \ddot\theta_b \end{aligned} \tag{30}$$

As shown in Fig. 2(b), let φ denote the angle made by the tangent to the Lamé curve, at an arbitrary point, with the X-axis. When the robot moves on the curve, according to Eqs. (9) and (19), the slope of the longitudinal line of the platform is expressed as

$$\tan\varphi = \frac{y_5'}{x_5'} = -\frac{t_\phi^2 - \cos(2\psi)}{\sin(2\psi)} \tag{31}$$

Upon differentiation of both sides of Eq. (31) with respect to time, one readily obtains

$$(1+\tan^2\varphi)\dot\varphi = -\frac{2t_\phi}{\sin(2\psi)}\dot t_\phi \tag{32}$$

As shown in Fig. 2(b), the time rate of change of the slope angle, $\dot\varphi$, actually amounts to the angular velocity of the DWMR, ω. Substitution of Eqs. (16) and (31) into Eq. (32) leads to

$$\dot t_\phi = \frac{t_\phi^2 - 2\cos(2\psi)t_\phi + 1}{2\sin(2\psi)t_\phi}\kappa_5 v_c \tag{33}$$

Upon substitution of Eqs. (24) and (33) into Eqs. (28), we obtain the time-derivative of the curvature in terms of t_ϕ:

$$\dot\kappa_5 = \frac{2k_3v_c\sin(2\psi)(1+t_\phi^3)^{5/3}(t_\phi^2 - 2\cos(2\psi)t_\phi + 1)}{l_2^2(t_\phi^4 - 2\cos(2\psi)t_\phi^2+1)^4} \tag{34}$$

Based on Eqs. (30), the actuated joint rates and their time rates of change have all been derived for the DWMR to track the transition trajectory at a given speed v_c. In order to calculate the motor torques, the inverse-dynamics model is formulated in section IV.

IV. TORQUE-SATURATION PREDICTION

A. ROBOT DYNAMICS

Within the Newton-Euler formulation applied to multibody systems, we distinguish three rigid bodies, one platform with two driving wheels, composing the DWMR, as shown in Fig. 1. The 6×6 *inertia dyad* [33] of the two driving wheels are denoted $\mathbf{M}_1$ and $\mathbf{M}_2$, with a corresponding notation for their six-dimensional twists, $\mathbf{t}_1$ and $\mathbf{t}_2$. Since the platform undergoes planar motion, its counterparts are the 3×3 dyad $\mathbf{M}_3'$ and the three-dimensional twist vector $\mathbf{t}_3'$. Besides, the linear transformation matrices of the three moving bodies are expressed as $\mathbf{T}_1$, $\mathbf{T}_2$ and $\mathbf{T}_3'$, which relate the body twists with the actuated joint rates, based on kinematics analysis [34]. There are

$$\begin{aligned} \mathbf{T}_1 &= \begin{bmatrix} -\mathbf{i} - r/(2l)\mathbf{k} & r/(2l)\mathbf{k} \\ r\mathbf{j} & \mathbf{0} \end{bmatrix} \\ \mathbf{T}_2 &= \begin{bmatrix} -r/(2l)\mathbf{k} & -\mathbf{i} + r/(2l)\mathbf{k} \\ \mathbf{0} & r\mathbf{j} \end{bmatrix} \\ \mathbf{T}_3' &= \frac{r}{2}\begin{bmatrix} -1/l & 1/l \\ (a/l)\mathbf{i} + \mathbf{j} & (-a/l)\mathbf{i} + \mathbf{j} \end{bmatrix} \end{aligned} \tag{35}$$

By means of the natural orthogonal complement [34], the generalized dynamics model is derived from the Newton-Euler equations for the DWMR, which leads to

$$\mathbf{I}\ddot{\boldsymbol\theta} = -\mathbf{C}\dot{\boldsymbol\theta} + \boldsymbol\tau + \boldsymbol\delta + \boldsymbol\gamma \tag{36}$$

where $\mathbf{I}$ is the positive-definite 2×2 generalized inertia matrix, $\mathbf{C}\dot{\boldsymbol\theta}$ being the 2-dimensional vector of Coriolis and centrifugal-force terms. Furthermore, $\boldsymbol\tau$, $\boldsymbol\delta$ and $\boldsymbol\gamma$ denote the 2-dimensional vectors of generalized active, dissipative, and gravity forces, respectively.

The 2×2 generalized inertia matrix $\mathbf{I}$ is obtained as

$$\mathbf{I} = \mathbf{I}_w + \mathbf{I}_p = \sum_{i=1}^{2}\mathbf{T}_i^T\mathbf{M}_i\mathbf{T}_i + (\mathbf{T}_3')^T\mathbf{M}_3'\mathbf{T}_3' \tag{37}$$

where $\mathbf{I}_w$ and $\mathbf{I}_p$ are the inertia matrices of the two driving wheels and of the platform, respectively.

In order to expand the foregoing matrices, we let I_x, I_y and I_z be the three principal moments of inertia of the two driving wheels, respectively. Moreover, I_3 denotes the scalar moment of inertia of the platform at its center of mass,

under planar motion. Therefore,

$$\mathbf{I}_i = \begin{bmatrix} I_x & 0 & 0 \\ 0 & I_y & 0 \\ 0 & 0 & I_z \end{bmatrix}, \quad \mathbf{M}_i = \begin{bmatrix} \mathbf{I}_i & \mathbf{O}_3 \\ \mathbf{O}_3 & m_i\mathbf{1}_3 \end{bmatrix}, \quad i = 1, 2$$
$$\mathbf{M}_3' = \begin{bmatrix} I_3 & \mathbf{0}_2^T \\ \mathbf{0}_2 & m_3\mathbf{1}_2 \end{bmatrix} \tag{38}$$

where $\mathbf{1}_2$ and $\mathbf{1}_3$ are the 2×2 and 3×3 identity matrices, respectively. Moreover, because of wheel symmetry, $I_x = I_y \equiv I$.

Substitution of Eqs. (35) and (38) into Eq. (37) leads to

$$\mathbf{I}_w = \begin{bmatrix} H_1 & H_2 \\ H_2 & H_1 \end{bmatrix}, \quad \mathbf{I}_p = \begin{bmatrix} H_3 & -H_3 \\ -H_3 & H_3 \end{bmatrix} \tag{39}$$

where H_1, H_2 and H_3 are given by

$$H_1 = I + \frac{1}{2}\left(\frac{r}{l}\right)^2 I_z + m_1 r^2, \quad H_2 = -\frac{1}{2}\left(\frac{r}{l}\right)^2 I_z$$
$$H_3 = \left(\frac{r}{2l}\right)^2 (I_3 + m_3 a^2) \tag{40}$$

Moreover, from Eqs. (30) and (39), we obtain the inertia-force term of the inverse-dynamics model, namely,

$$\mathbf{I}\ddot{\boldsymbol{\theta}} = (\mathbf{I}_w + \mathbf{I}_p)\ddot{\boldsymbol{\theta}}_a = \begin{bmatrix} H_4\ddot{\theta}_a + H_5\ddot{\theta}_b \\ H_4\ddot{\theta}_a - H_5\ddot{\theta}_b \end{bmatrix} \equiv \begin{bmatrix} f_1 \\ f_2 \end{bmatrix} \tag{41}$$

where H_4 and H_5 are defined below:

$$H_4 \equiv H_1 + H_2 = I + m_1 r^2,$$
$$H_5 \equiv H_1 - H_2 + 2H_3$$
$$= I + (\frac{r}{l})^2 I_z + m_1 r^2 + \frac{1}{2}(\frac{r}{l})^2 (I_3 + m_3 a^2) \tag{42}$$

The coefficient matrix $\mathbf{C}$ can be expanded in a similar way. When the time histories of the actuated joint rates are given, the torque requirements at the different actuated joints are determined.

Moreover, the dissipative-force term of the inverse-dynamics model, associated with linearly viscous effects, is linear in the vector of actuated joint rates, i.e.,

$$\boldsymbol{\delta} = -\beta\dot{\boldsymbol{\theta}} \tag{43}$$

where β is the coefficient of viscous friction.

B. PEAK-TORQUE POSITIONING

Although the foregoing Lamé-curve trajectory is planned geometrically with G^2-continuity, it is not essentially guaranteed that the robot motors will be able to supply the torques required by the turning maneuvers. If any of the computed torques, τ_i $(i = 1, 2)$, exceeds the rated torque τ_r, the transition trajectory is then unfeasible. In order to find the peak torque required on the transition trajectory, the maximum curvature and its rate of change (RoC) should be computed in advance.

Since the transformation of the Lamé curve in step 2 is symmetrical with respect to the Y-axis, the shape, the trajectory curvature κ_5 and its RoC $\dot{\kappa}_5$ follow this symmetry about the midpoint, as shown in Fig. 5. Apparently, when

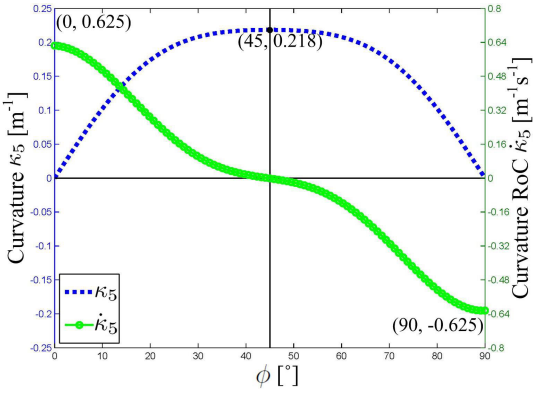

FIGURE 5. The curvature and its RoC for the Lamé-curve trajectory of Fig. 4.

$\phi = 0$ or $\pi/2$, the curvature vanishes, i.e., $\kappa_5(0) = 0$ and $\kappa_5(\pi/2) = 0$, while its RoC attains extreme values, i.e., $\dot{\kappa}_5(0) = \dot{\kappa}_{\max}$ and $\dot{\kappa}_5(\pi/2) = -\dot{\kappa}_{\max}$. When $\phi = \pi/4$, the curvature attains its maximum value, $\kappa_5(\pi/4) = \kappa_{\max}$, while its RoC vanishes.

According to Eqs. (23) and (34), the maximum curvature and its RoC are calculated as

$$\kappa_{\max} = \frac{2^{5/6}\sin 2\psi}{l_2(1-\cos 2\psi)^{3/2}}, \quad \dot{\kappa}_{\max} = \frac{2v_c \sin 2\psi}{l_2^2} \tag{44}$$

When the DWMR moves along a Lamé-curve trajectory towards path 2 at a constant speed v_c, the actuated joint rates are $\dot{\theta}_1 = v_c(1 + l\kappa_5)/r$ and $\dot{\theta}_2 = v_c(1 - l\kappa_5)/r$, implying that the dissipative force of one driving wheel increases while that of the other wheel decreases. Which wheel needs a higher torque depends on whether the DWMR is turning left or right. Since $\dot{v}_c = 0$, the corresponding time-derivatives are $\ddot{\theta}_1 = v_c l\dot{\kappa}_5/r$ and $\ddot{\theta}_2 = -v_c l\dot{\kappa}_5/r$.

At the starting point of the transition trajectory, $\kappa_5(0) = 0$ and $\dot{\kappa}_5(0) = \dot{\kappa}_{\max}$. Hence, $\dot{\theta}_1(0) = \dot{\theta}_2(0) = v_c/r$. Since $\ddot{\theta}_1(0) = v_c l\dot{\kappa}_{\max}/r$ and $\ddot{\theta}_2(0) = -v_c l\dot{\kappa}_{\max}/r$, the inertia forces are $f_1(0) = H_5\, v_c l\dot{\kappa}_{\max}/r$ and $f_2(0) = -H_5\, v_c l\dot{\kappa}_{\max}/r$, which require higher motor torques.

At the midpoint of the transition trajectory, $\kappa_5(\pi/4) = \kappa_{\max}$ and $\dot{\kappa}_5(\pi/4) = 0$. Thus, the inertia-force term vanishes, while $\dot{\theta}_1(\pi/4) = v_c(1 + l\kappa_{\max})/r$, $\dot{\theta}_2(\pi/4) = v_c(1 - l\kappa_{\max})/r$, thus resulting in an additional dissipative-force term, $\delta_0(\pi/4) = \beta v_c l\kappa_{\max}/r$.

Therefore, the point on the trajectory, at which the peak torque is needed, is determined by comparison of the magnitudes of the additional inertia-force term $f_1(0)$ and the additional dissipative-force term $\delta_0(\pi/4)$. Let λ denote the ratio of the magnitude of these two terms:

$$\lambda = \left|\frac{f_1(0)}{\delta_0(\pi/4)}\right| = \left|\frac{H_5\dot{\kappa}_{\max}}{\beta\kappa_{\max}}\right| = k_4\left|\frac{H_5 v_c}{\beta l_2}\right| \tag{45}$$

where k_4 is defined as

$$k_4 \equiv 2^{1/6}(1 - \cos 2\psi)^{3/2} \tag{46}$$

with $k_4 > 1$ for all $\psi \in [\pi/4, 3\pi/4]$.

For most common mobile robots, the inertia coefficient and speed term $H_5\ v_c$ is usually greater than the friction coefficient and the geometrical term βl_2. As a result, a peak torque is required at the starting point of the trajectory. If the DWMR turns right, i.e., $\psi \in [\pi/4, \pi/2)$, then the left driving wheel needs the peak torque, i.e., $\tau_1(0) = \tau_{\max}$. When $\psi \in (\pi/2, 3\pi/4]$, the right wheel needs the peak torque, i.e., $\tau_2(0) = \tau_{\max}$.

For the right-turning trajectory shown in Fig. 4, the left motor is saturated if the computed torque of the left driving wheel at the starting point is higher than the rated torque, i.e., $\tau_1(0) > \tau_r$. Obviously, the magnitude of the actuated joint rates and their time-derivatives, $\dot{\theta}_1(0)$, $\dot{\theta}_2(0)$, $\ddot{\theta}_1(0)$ and $\ddot{\theta}_2(0)$, are all proportional to the given speed v_c. In this sense, the DWMR tracking the transition trajectory at a low velocity v_c only needs low torques τ_i. However, this low speed should achieve a constant value before the robot arrives at the first blending point.

If the current travelling speed v_c at the starting point has already caused motor saturation, it is impossible for the robot to mitigate the saturation even if its speed is reduced immediately. Let us assume that the robot begins to decrease its speed v_c by means of a deceleration profile from the starting point. Since $\kappa_5(0) = 0$ and $\dot{\kappa}_5(0) = \dot{\kappa}_{\max}$, the dissipative forces remain the same as those on the straight path, while the inertia forces are $f_1(0) = H_4\dot{v}_c/r + H_5\ v_c l\dot{\kappa}_{\max}/r$ and $f_2(0) = H_4\dot{v}_c/r - H_5\ v_c l\dot{\kappa}_{\max}/r$. Compared with the inertia forces needed at a constant speed v_c, an extra inertia-force term $H_4\dot{v}_c/r$ is caused by the deceleration profile, which requires even higher motor torques than at a constant speed, thereby exacerbating motor saturation.

V. TORQUE-SATURATION AVOIDANCE

From the above analysis follows that motor saturation is unavoidable when the DWMR moves along a Lamé-curve trajectory with a high curvature at a high speed. Therefore, the robot should begin a Lamé-curve trajectory towards path 2 before its curvature becomes too high, else the speed should be decreased to a suitable level before the robot enters the transition trajectory. These two torque limitation schemes are both based on saturation prediction, i.e., anticipating whether a particular curvature or speed will result in motor saturation, and moreover, preventing it by adjusting the robot actions appropriately in advance.

The first torque limitation scheme can be used to determine the position of the first blending point C on path 1, as shown in Fig. 4. It is not difficult to analyze the relation between the maximum curvature and its RoC, $\kappa_{\max}$ and $\dot{\kappa}_{\max}$, with the distance l_2 of the first blending point C and the intersection point M_k. According to Eqs. (44), the magnitudes of $\kappa_{\max}$ and $\dot{\kappa}_{\max}$ are inversely proportional to l_2. In Fig. 4, if the DWMR continues to travel along path 1 instead of switching to a Lamé-curve trajectory, l_2 decreases gradually, which tends to make $|\kappa_{\max}|$ and $|\dot{\kappa}_{\max}|$ higher. Hence, motor saturation definitely occurs when the distance l_2 becomes too small. On the other hand, it is not necessary for the robot to start a Lamé-curve trajectory prematurely when the distance l_2 is significantly large, as this kind of turning maneuvers have a low motion efficiency.

Taking both aspects into account, it is reasonable to set the upper and lower limits of the distance l_2 for trajectory generation based on Lamé-curve blending. The fundamental criterion relies on robot dynamics and motor torques. For given robot motors, the lower and upper threshold of motor torques, τ_a and τ_b, are prescribed with respect to the rated torque, τ_r. An iterative r-step saturation-avoidance prediction planning strategy is illustrated in Fig. 6.

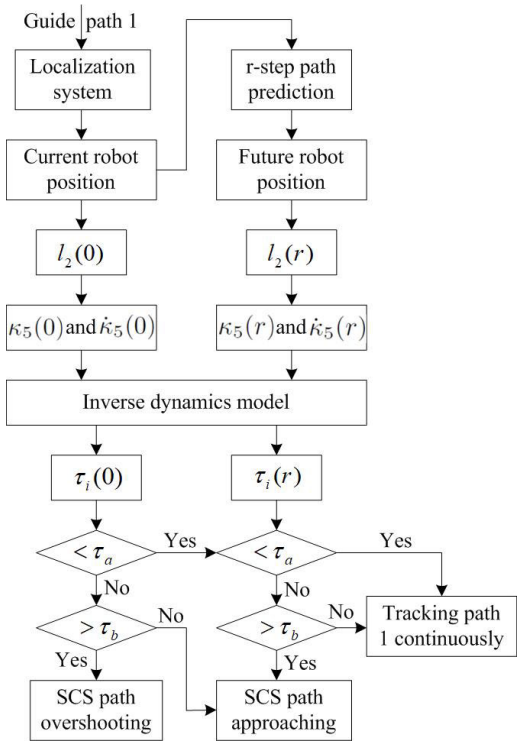

FIGURE 6. Saturation-avoidance prediction strategy.

When the localization system measures the current position of the robot on path 1, the distance $l_2(0)$ is used as the time-varying parameter for affine transformations of a Lamé curve to blend paths 1 and 2. Then, the maximum magnitudes of the Lamé-curve trajectory curvature and its RoC, $\kappa_5(0)$ and $\dot{\kappa}_5(0)$, are calculated by means of Eqs. (44). Thirdly, the inverse dynamics model is utilized to compute the motor torques $\tau_i(0)$ required.

Meanwhile, the future position of the robot on path 1 is estimated in the next r-step control instants. The distance $l_2(r)$ is employed to generate a new Lamé-curve trajectory, and then $\kappa_5(r)$, $\dot{\kappa}_5(r)$ and $\tau_i(r)$ are calculated accordingly. Furthermore, several different robot actions are carried out, based on the relation between the computed torques and their thresholds.

(1) If $\tau_a \le \tau_i(0) \le \tau_b$, the currently required torques lie within the suitable torque range. Hence, the robot can follow the Lamé-curve trajectory properly, without motor saturation.

(2) If $\tau_i(0) > \tau_b$, the computed torques exceed the upper threshold of motor torque. Motor saturation is inevitable, no matter whether a deceleration profile is taken. Consequently, the robot cannot track the trajectory closely, thereby resulting in overshooting on the SCS turning path.

(3) If $\tau_i(0) < \tau_a$, compare the torques, $\tau_i(r)$, anticipated after r steps, with the torque thresholds. $\tau_i(r) > \tau_b$ implies that motor saturation will occur at the upcoming instant. In order to avoid this, the robot should change to the Lamé-curve trajectory immediately at the current instant. If $\tau_i(r) \leq \tau_b$, the robot should keep moving along path 1 instead of trajectory switching, thus resulting in a continuous decrease of l_2.

On the other hand, the deceleration control scheme can be employed additionally, if the robot runs in a cramped space that does not allow for a large turning radius. In order to avoid motor saturation, a deceleration profile is to be adopted on path 1 before the robot enters the Lamé-curve trajectory. A non-dimensional 3-4-5 polynomial is used as the profile [34], namely,

$$p(s) = 6s^5 - 15s^4 + 10s^3 \tag{47}$$

for $s \in [0, 1]$, to ensure that its first and second derivatives are both smooth, vanishing at the two ends of the interval [0,1].

Let v_1 and v_2 denote the previous and the new constant speed, the former being reduced to the latter in a period T_d. Thus, the deceleration profile is designed as

$$v_c(t) = v_1 + (v_2 - v_1)p\Big(\frac{t}{T_d}\Big) \tag{48}$$

for $t \in [0, T_d]$.

Moreover, the time-derivative of the speed function is

$$\dot{v}_c(t) = (v_2 - v_1)\frac{30}{T_d}\Big[\Big(\frac{t}{T_d}\Big)^4 - 2\Big(\frac{t}{T_d}\Big)^3 + \Big(\frac{t}{T_d}\Big)^2\Big] \tag{49}$$

The actuated joint rates and their time-derivatives are then obtained by substituting Eqs. (48) and (49) into Eqs. (26) and (27). Finally, the time-histories of motor torques τ_i can be computed based on the inverse-dynamics model, Eq. (36).

VI. SIMULATION TESTS

In order to validate the foregoing iterative Lamé-trajectory planning scheme for motor-saturation avoidance of a robot upon turning maneuvers, a circular arc and a set of affine-transformed Lamé curves are used to generate SCS turning paths. Then, the peak torques of the two driving wheels are calculated by means of the computed-torque method, based on the inverse-dynamics model. Lastly, the torque-saturation avoidance schemes are implemented by adjusting trajectory curvature and robot speed according to a r-step prediction planning strategy. The geometric, kinematic and inertial parameters of the DWMR at hand are given in Tables 1 and 2. Moreover, the friction coefficient is $\beta = 2$ Ns/rad. The rated torque of the onboard motors is $\tau_r = 20$ Nm, while the upper and lower threshold of motor torques

TABLE 1. Geometric and kinematic parameters.

r [m]	l [m]	a [m]	b [m]	v_c [m/s]
0.08	0.2	0.18	0.42	0.5

TABLE 2. Inertial parameters.

m_1	2 kg	I_x	0.0064 kg.m^2	I_y	0.0032 kg.m^2
m_2	2 kg	I_z	0.0032 kg.m^2	I_3	104 kg.m^2
m_3	200 kg	H_4	0.0192 kg.m^2	H_5	8.8581 kg.m^2

are $\tau_a = 6$ Nm and $\tau_b = 20$ Nm. In fact, for the sake of reliable torque-saturation avoidance, a more conservative value, i.e., significantly lower than the rated torque, can be used as the upper threshold τ_b, if external disturbance, model nonlinearity and parameter uncertainty are all taken into account.

A. BLENDING CURVE SCHEME

As shown in Fig. 2(b), let us assume that paths 1 and 2 intersect at point M_k, with $\psi = 60°$ and $l_2 = 1.6$ m. The transition trajectory for a robot to transfer from path 1 to path 2 is obtained by means of different curves: one is a circular arc, the other an affine-transformed Lamé curve. The trajectory curvature and its RoC are illustrated for the two curves in Figs. 7 and 5, respectively.

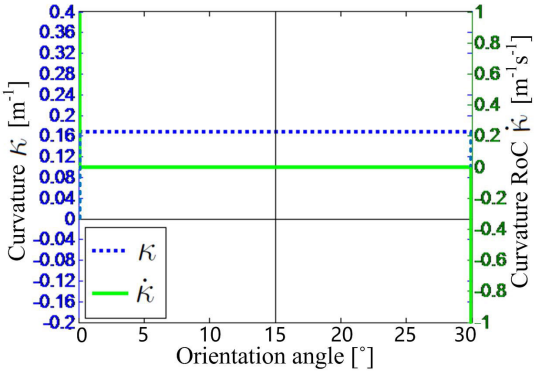

FIGURE 7. The curvature and its RoC for the circular arc.

In Fig. 7, the curvature κ of the circular arc has a positive step change at the starting point—corresponding to the first blending point C of the SCS path in Fig. 2(b), followed by a negative step change at the ending point—corresponding to the second blending point T_k of the SCS path, and a constant value on the trajectory in-between. On the contrary, in Fig. 5, the curvature κ_5 of the Lamé curve has a smooth increment from the starting point, to a significantly flat section at the middle point, followed by a smooth decrement from the middle point to the ending point. Consequently, one positive and one negative impulses occur on the curvature RoC $\dot{\kappa}$ for the circular arc at these two end-points, while the curvature RoC $\dot{\kappa}_5$ of the Lamé curve remains smooth, with finite initial and terminal values.

For a constant speed, $v_c = 0.5$ m/s, the actuated joint rates and their time-derivatives on different trajectories are calculated based on Eqs. (26) and (27). Then, the required torques of the two driving wheels are computed for the DWMR by means of the inverse-dynamics model, Eq. (36), as shown in Figs. 8 and 9, respectively.

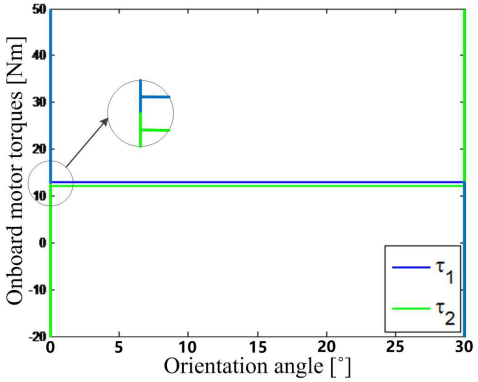

FIGURE 8. Required motor torques of the DWMR on the circular arc.

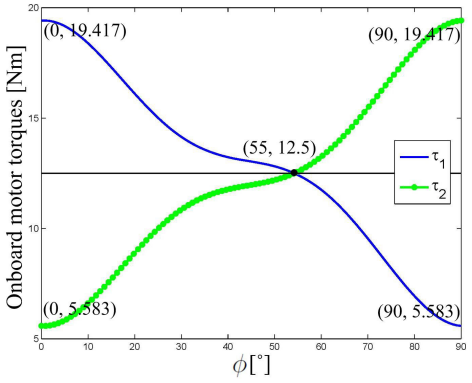

FIGURE 9. Required motor torques of the DWMR on the Lamé curve.

In Fig. 8, the motor torque of the left wheel has a positive impulse at the starting point, a negative impulse at the ending point, and a constant value on the trajectory in-between. It is noteworthy that the amplitude of the torque impulse is higher than 50 Nm, exceeding the rated torque of robot motors. On the contrary, in Fig. 9, the motor torque of the left wheel for the Lamé curve is always smooth, its amplitude remaining below the rated torque.

B. CURVATURE-BOUNDED SCHEME

As mentioned above, a series of Lamé-curve trajectories can be obtained on the basis of the robot position on path 1 or, more accurately, of the distance of the robot to the intersection point, l_2. The curvature and its RoC in Fig. 5 are calculated for the Lamé-curve trajectory with $l_2 = 1.6$ m. If the robot does not initiate the Lamé-curve trajectory at that point until it arrives at a closer position where $l_2 = 1$ m, the curvature and its RoC for the new Lamé-curve trajectory are illustrated in Fig. 10. Compared with Fig. 5, the new Lamé curve has a higher curvature and RoC, implying that the robot will make a sharper turning maneuver.

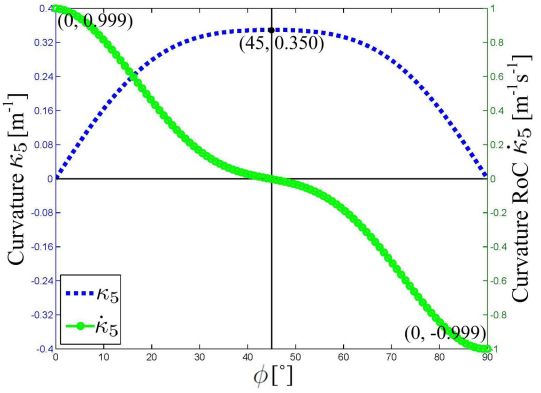

FIGURE 10. The curvature and its RoC for the Lamé curve with $l_2 = 1$ m.

For a constant speed, $v_c = 0.5$ m/s, the actuated joint rates and their time-derivatives for the robot traveling on different Lamé curves, with $l_2 = 1.6$ m and $l_2 = 1$ m, are shown in Figs. 11 and 12, respectively. Obviously, due to a higher curvature of the new Lamé curve, the maximum actuated joint rate of the left driving wheel increases from 6.523 to 6.687 rad/s, its maximum time-derivative rising from 0.781 to 1.249 rad/s^2.

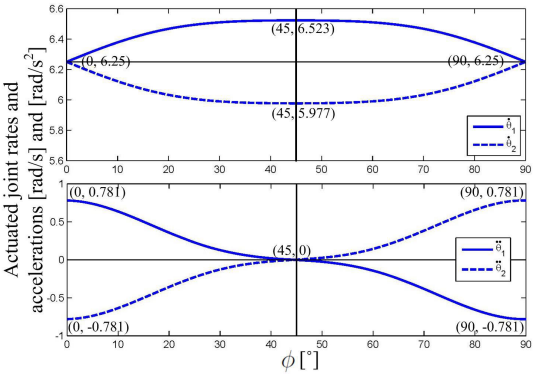

FIGURE 11. Actuated joint rates and accelerations on the Lamé curve with $l_2 = 1.6$ m.

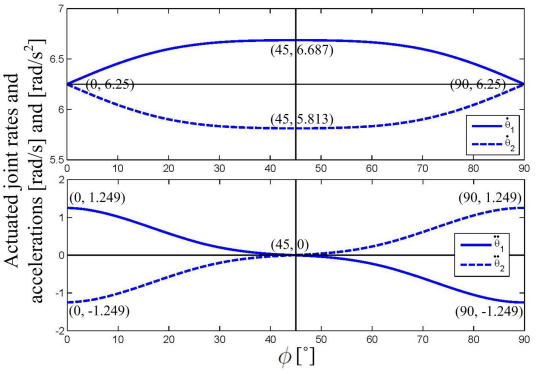

FIGURE 12. Actuated joint rates and accelerations on the Lamé curve with $l_2 = 1$ m.

Consequently, higher motor torques are required by the robot to track the new Lamé-curve trajectory of higher curvature, as shown in Fig. 13. The peak motor torque of the left driving wheel increases from 19.417 to 23.567 Nm, which exceeds the rated motor torque. In order to avoid motor saturation, the r-step prediction planning strategy is to be implemented online iteratively, before the robot reaches the dangerous position where $l_2 = 1$ m, as shown in Fig. 6.

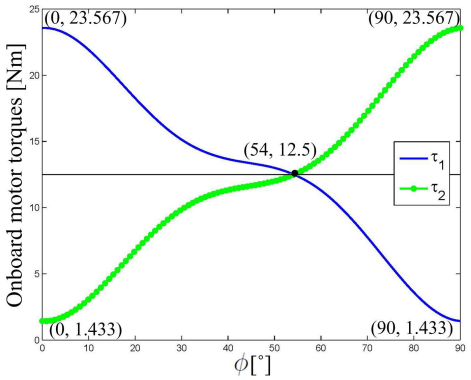

FIGURE 13. Required motor torques of the DWMR on the Lamé curve with $l_2 = 1$ m.

The first torque limitation scheme is based on restricting the Lamé-curve curvature and its RoC, by determining the position of the first blending point on path 1. In fact, when the robot moves along path 1, the current distance $l_2(0)$ is detected as the time-varying parameter for its turning maneuver, consisting of curve blending, trajectory planning and torque computation. Meanwhile, the distance $l_2(r)$ is estimated in the next r-step control instants, in order to verify whether motor saturation will eventually occur. Hence, both current motor torques $\tau_i(0)$ and their future values $\tau_i(r)$ are predicted accordingly.

Let us assume that the robot arrives at the location where $l_2 = 1.6$ m, and its position and state 1.2s later are predicted. As shown in Figs. 9 and 13, $\tau_a \leq \tau_i(0) \leq \tau_b$, but $\tau_i(r) > \tau_b$. This implies that if the robot initiates the Lamé-curve trajectory at the current position, it will have an efficient and saturation-free transition trajectory; otherwise, motor saturation will occur 1.2s later, when the robot enters a sharper Lamé-curve trajectory. According to the iterative r-step prediction planning strategy, shown in Fig. 6, the most appropriate action for the robot is to begin the Lamé-curve trajectory at the current position immediately.

C. VELOCITY-BOUNDED SCHEME

The second torque limitation scheme aims to decrease the actuated joint rates and accelerations for the robot moving on Lamé curves of higher curvature, by reducing the traveling speed. Let us assume that, when $l_2 = 1$ m, the robot initiates the sharper Lamé-curve trajectory at a lower speed, $v_c = 0.4$ m/s. Since the lower speed does not change the geometric attributes of trajectory planning, the transition trajectory remains the Lamé curve of identical shape and curvature, as shown in Fig. 10. However, the kinematic and dynamic attributes of the trajectory depend on the robot speed. The actuated joint rates, their time-derivatives, and the required motor torques are recalculated accordingly, as shown in Figs. 14 and 15.

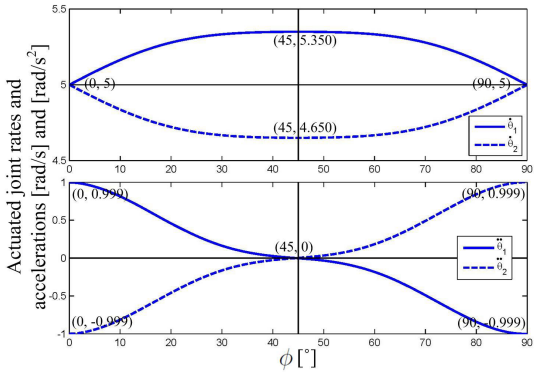

FIGURE 14. Actuated joint rates and accelerations of the DWMR at a lower speed $v_c = 0.4$ m/s.

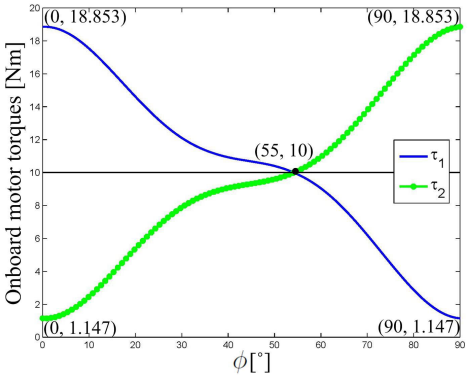

FIGURE 15. Required motor torques of the DWMR at a lower speed $v_c = 0.4$ m/s.

Comparing Figs. 11, 12 and 14, we can find some meaningful results: (1) since the curvature of the starting point on the transition trajectory vanishes, the actuated joint rates depend only on the robot speed, i.e., 6.25 rad/s in Figs. 11 and 12 for a high speed $v_c = 0.5$ m/s, while 5 rad/s in Fig. 14 for a low speed $v_c = 0.4$ m/s; (2) due to the differential driving model, the actuated joint rates of the robot are symmetric about their average value, which is also determined by the robot speed, i.e., 6.25 rad/s for $v_c = 0.5$ m/s while 5 rad/s for $v_c = 0.4$ m/s; and (3) the accelerations of the driving wheels are influenced by both v_c and $\dot{\kappa}_5$, so that they attain the maximum value, 1.249 rad/s^2, in Fig. 12, because of both high robot speed and high curvature RoC.

Moreover, similar dynamics results can be drawn by analyzing Figs. 9, 13 and 15. (1) Due to the differential driving model, the motor torques of the two driving wheels are symmetric about their average value, which is determined by the robot speed as well, 12.5 Nm in Figs. 9 and 13 for $v_c = 0.5$ m/s while 10 Nm in Fig. 15 for $v_c = 0.4$ m/s. (2) The peak torque depends on both the maximum curvature

RoC $\dot{\kappa}_{\max}$ and the robot speed v_c. For motor saturation, occurring in Fig. 13, two different torque limitation schemes can be adopted, in order to bring the highest motor torque below the upper threshold τ_b. One scheme is oriented to the trajectory curvature, beginning a Lamé-curve trajectory earlier when the corresponding curvature is still low, as shown in Fig. 9. The other scheme focuses on the deceleration, slowing down the robot to a low constant speed before it enters the Lamé-curve trajectory, as shown in Fig. 15.

The simulation tests validate the effectiveness of the iterative Lamé-trajectory planning scheme to avoid motor saturation for turning maneuvers of a robot moving on SCS paths. It is noteworthy that when the curvature-bounded scheme is used to decrease the peak motor torques of the two driving wheels, the robot has to adopt a larger turning radius, which requires more free space in the surroundings.

It should be pointed out that only trajectory shape and robot speed are considered as the main factors for motor-saturation avoidance in the iterative Lamé-trajectory planning scheme. Other factors, such as external disturbances, model nonlinearity and parameter uncertainty, are not included explicitly in our planning scheme. Hence, it is advisable to use a robust trajectory tracking control approach, following our planning scheme, to handle these factors.

VII. CONCLUSIONS

Schemes for actuator-saturation avoidance in mobile robots are mainly oriented to torque-bounded controller design or curvature-bounded trajectory planning. As the causes of actuator saturation are not always known or predictable, many constrained control strategies have been used to cope with external disturbances, model nonlinearity and parameter uncertainty. However, the dominant factor for actuator saturation can be estimated in some specific operation scenarios. For example, the shape and curvature of the transition trajectory influence the robot state significantly in turning maneuvers between two straight paths.

In order to avoid motor saturation in turning maneuvers, an iterative Lamé-trajectory planning scheme is proposed that offers a smooth curvature-bounded transition trajectory for tracking control of mobile robots. Firstly, a smooth G^2-continuous transition trajectory is generated by means of a Lamé-curve blending procedure based on affine transformations. Then, a peak-torque positioning technique is formulated to estimate the peak torques of the robot on the trajectory, by combining the computed-torque method and the inverse-dynamics model. Finally, a saturation-avoidance trajectory planning strategy is developed to suppress the peak torques, by means of the r-step prediction procedure and two torque limitation schemes. One scheme restricts the Lamé-curve curvature by determining the positions of the blending points, while the other decreases the actuated joint rates by reducing the robot speed. Simulation tests validate the effectiveness of our scheme for torque-saturation avoidance in turning maneuvers.

In future research work, our trajectory planning scheme will be integrated with a robust trajectory tracking control method. The effectiveness of torque-saturation avoidance is further verified on a robot under external disturbances, model nonlinearity and parameter uncertainty.

REFERENCES

[1] A. Kelly, B. Nagy, and D. Stager, "An infrastructure-free automated guided vehicle based on computer vision," *IEEE Robot. Autom. Mag.*, vol. 14, no. 3, pp. 24–34, Sep. 2007.

[2] X. Wu, Y. Zhang, T. Zou, L. Zhao, P. Lou, and Z. Yin, "Coordinated path tracking of two vision-guided tractors for heavy-duty robotic vehicles," *Robot. Comput.-Integr. Manuf.*, vol. 53, no. 10, pp. 93–107, Oct. 2018.

[3] X. Lyu, Y. Song, C. He, Q. Lei, and W. Guo, "Approach to integrated scheduling problems considering optimal number of automated guided vehicles and conflict-free routing in flexible manufacturing systems," *IEEE Access*, vol. 7, pp. 74909–74924, 2019.

[4] A. Vale, R. Ventura, P. Lopes, and I. Ribeiro, "Assessment of navigation technologies for automated guided vehicle in nuclear fusion facilities," *Robot. Auto. Syst.*, vol. 97, pp. 153–170, Nov. 2017.

[5] F. Heidari and R. Fotouhi, "A human-inspired method for point-to-point and path-following navigation of mobile robots," *J. Mech. Robot.*, vol. 7, no. 4, Nov. 2015, Art. no. 041025.

[6] H. Martínez-Barberá and D. Herrero-Pérez, "Autonomous navigation of an automated guided vehicle in industrial environments," *Robot. Comput.-Integr. Manuf.*, vol. 26, no. 4, pp. 296–311, Aug. 2010.

[7] M. Seder, M. Baotic, and I. Petrovic, "Receding horizon control for convergent navigation of a differential drive mobile robot," *IEEE Trans. Control Syst. Technol.*, vol. 25, no. 2, pp. 653–660, Mar. 2017.

[8] B. B. K. Ayawli, X. Mei, M. Shen, A. Y. Appiah, and F. Kyeremeh, "Mobile robot path planning in dynamic environment using Voronoi diagram and computation geometry technique," *IEEE Access*, vol. 7, pp. 86026–86040, 2019.

[9] T. Zou, J. Angeles, and F. Hassani, "Dynamic modeling and trajectory tracking control of unmanned tracked vehicles," *Robot. Auto. Syst.*, vol. 110, pp. 102–111, Dec. 2018.

[10] K. Shojaei, A. M. Shahri, A. Tarakameh, and B. Tabibian, "Adaptive trajectory tracking control of a differential drive wheeled mobile robot," *Robotica*, vol. 29, no. 3, pp. 391–402, May 2011.

[11] S. G. Tzafestas, K. M. Deliparaschos, and G. P. Moustris, "Fuzzy logic path tracking control for autonomous non-holonomic mobile robots: Design of system on a chip," *Robot. Auto. Syst.*, vol. 58, no. 8, pp. 1017–1027, Aug. 2010.

[12] X. Wu, W. Shen, P. Lou, B. Wu, L. Wang, and D. Tang, "An automated guided mechatronic tractor for path tracking of heavy-duty robotic vehicles," *Mechatronics*, vol. 35, no. 5, pp. 23–31, May 2016.

[13] M. H. Ko, B.-S. Ryuh, K. C. Kim, A. Suprem, and N. P. Mahalik, "Autonomous greenhouse mobile robot driving strategies from system integration perspective: Review and application," *IEEE/ASME Trans. Mechatronics*, vol. 20, no. 4, pp. 1705–1716, Aug. 2015.

[14] W. Xing, L. Peihuang, Y. Jun, Q. Xiaoming, and T. Dunbing, "Intersection recognition and guide-path selection for a vision-based AGV in a bidirectional flow network," *Int. J. Adv. Robotic Syst.*, vol. 11, no. 3, p. 39, Mar. 2014.

[15] J.-L. Yang, D.-T. Su, Y.-S. Shiao, and K.-Y. Chang, "Path-tracking controller design and implementation of a vision-based wheeled mobile robot," *Proc. Inst. Mech. Eng. I, J. Syst. Control Eng.*, vol. 223, no. 6, pp. 847–862, Sep. 2009.

[16] R. Fierro and F. L. Lewis, "Control of a nonholonomic mobile robot using neural networks," *IEEE Trans. Neural Netw.*, vol. 9, no. 4, pp. 589–600, Jul. 1998.

[17] Y. Kim and B. K. Kim, "Efficient time-optimal two-corner trajectory planning algorithm for differential-driven wheeled mobile robots with bounded motor control inputs," *Robot. Auto. Syst.*, vol. 64, pp. 35–43, Feb. 2015.

[18] C.-L. Hwang, "Comparison of path tracking control of a car-like mobile robot with and without motor dynamics," *IEEE/ASME Trans. Mechatronics*, vol. 21, no. 4, pp. 1801–1811, Aug. 2016.

[19] C. J. Fallaha, M. Saad, H. Y. Kanaan, and K. Al-Haddad, "Sliding-mode robot control with exponential reaching law," *IEEE Trans. Ind. Electron.*, vol. 58, no. 2, pp. 600–610, Feb. 2011.

[20] Y. Xu, "Chattering free robust control for nonlinear systems," *IEEE Trans. Control Syst. Technol.*, vol. 16, no. 6, pp. 1352–1359, Nov. 2008.
[21] J.-Y. Zhai and Z.-B. Song, "Adaptive sliding mode trajectory tracking control for wheeled mobile robots," *Int. J. Control*, vol. 92, no. 10, pp. 2255–2262, Oct. 2019.
[22] K. B. Kim and B. K. Kim, "Minimum-time trajectory for three-wheeled omnidirectional mobile robots following a bounded-curvature path with a referenced heading profile," *IEEE Trans. Robot.*, vol. 27, no. 4, pp. 800–808, Aug. 2011.
[23] G. Indiveri, "Swedish wheeled omnidirectional mobile robots: Kinematics analysis and control," *IEEE Trans. Robot.*, vol. 25, no. 1, pp. 164–171, Feb. 2009.
[24] C. Guarino Lo Bianco, "Minimum-jerk velocity planning for mobile robot applications," *IEEE Trans. Robot.*, vol. 29, no. 5, pp. 1317–1326, Oct. 2013.
[25] K. D. Do, "Bounded controllers for global path tracking control of unicycle-type mobile robots," *Robot. Auto. Syst.*, vol. 61, no. 8, pp. 775–784, Aug. 2013.
[26] X. Jin, J. Qin, Y. Shi, and W. X. Zheng, "Auxiliary fault tolerant control with actuator amplitude saturation and limited rate," *IEEE Trans. Syst., Man, Cybern., Syst.*, vol. 48, no. 10, pp. 1816–1825, Oct. 2018.
[27] I.-H. Li, Y.-H. Chien, W.-Y. Wang, and Y.-F. Kao, "Hybrid intelligent algorithm for indoor path planning and trajectory-tracking control of wheeled mobile robot," *Int. J. Fuzzy Syst.*, vol. 18, no. 4, pp. 595–608, Aug. 2016.
[28] X. Wu, P. Jin, T. Zou, Z. Qi, H. Xiao, and P. Lou, "Backstepping trajectory tracking based on fuzzy sliding mode control for differential mobile robots," *J. Intell. Robotic Syst.*, vol. 96, no. 1, pp. 109–121, Oct. 2019.
[29] J. J. Risler, *Mathematical Methods for CAD*. Cambridge, U.K.: Cambridge Univ. Press, 1992.
[30] X. Wu, J. Angeles, T. Zou, C. Sun, Q. Sun, and L. Wang, "Receding-horizon vision guidance with smooth trajectory blending in the field of view of mobile robots," *Appl. Sci.*, vol. 10, no. 2, p. 676, 2020.
[31] X. Wu, J. Angeles, T. Zou, H. Xiao, W. Li, and P. Lou, "Steering-angle computation for the multibody modelling of differential-driving mobile robots with a caster," *Int. J. Adv. Robotic Syst.*, vol. 15, no. 6, Nov. 2018, Art. no. 172988141882016.
[32] L. Brand, *Advanced Calculus*. New York, NY, USA: Wiley, 1965.
[33] R. V. Mises, "Motorrechnung, ein neues hilfsmittel der mechanik," *ZAMM Zeitschrift für Angew. Math. Mech.*, vol. 4, no. 2, pp. 155–181, 1924.
[34] J. Angeles, *Fundamentals of Robotic Mechanical Systems: Theory, Methods, and Algorithms*, 4th ed. New York, NY, USA: Springer, 2014.

XING WU received the B.Eng. and Ph.D. degrees in mechanical engineering from the Nanjing University of Aeronautics and Astronautics (NUAA), Nanjing, China, in 2004 and 2010, respectively. In 2010, he joined the College of Mechanical and Electrical Engineering, NUAA, where he is currently an Associate Professor. He was a Visiting Professor with the Centre for Intelligent Machines, McGill University, Canada, from November 2016 to November 2017. His research interests include intelligent sensing and control; design, guidance, navigation, and control of mobile robots; and coordinated control and intelligent scheduling of multirobot systems. He has authored or coauthored about 40 journal articles and conference papers and obtained more than 20 issued Chinese patents. He received the Second Prize for Progress in Science and Technology, Ministry of Education of China, in 2013 and 2017.

JORGE ANGELES (Life Fellow, IEEE) received the Engineering Diploma degree in electromechanical engineering and the M.Eng. degree in mechanical engineering from the Universidad Nacional Autonoma de México (UNAM), Mexico City, in 1969 and 1970, respectively, and the Ph.D. degree in applied mechanics from Stanford University, in 1973. In 1984, he joined the Department of Mechanical Engineering, McGill University, Montreal, after 11 years of teaching at UNAM. In 1985, he became a Founding Member of the Centre for Intelligent Machines, McGill. Since September 2017, he has been the Professor Emeritus of mechanical engineering. He is one of the 12 honorary members of IFToMM and a Fellow of The Royal Society of Canada, the Canadian Society for Mechanical Engineers, ASME, and the Canadian Academy of Engineering.

TING ZOU received the B.Sc. degree in electrical engineering and the M.Sc. degree in automatic control engineering from Xi'an Jiaotong University, China, in 2005 and 2008, respectively, and the Ph.D. degree from McGill University, in 2013. She proposed a novel bi-axial accelerometer design based on microelectromechanical (MEMS) techniques and its strapdowns, to improve current pose-and-twist estimation in McGill University. Afterwards, she joined the Centre for Intelligent Machines, McGill University, as a Postdoctoral Fellow, working on optimum design of the next-generation transmissions for electric vehicles and trajectory tracking and motion control of autonomous tracked vehicles for mining blasthole drilling rigs. She is currently an Assistant Professor with the Department of Mechanical Engineering, Memorial University of Newfoundland, Canada. Her current research interests include mechanism design and control of bio-inspired robotic mechanical systems and MEMS systems.

JUNJIE YANG received the B.E. degree in mechatronics from Nanjing Forestry University, China, in 2019. He is currently pursuing the M.S. degree in mechanical engineering with the Nanjing University of Aeronautics and Astronautics, China. His current research interest includes control and scheduling of robotic systems.

HONGKAI LI received the B.S. degree in mechanical engineering from Central South University, Changsha, China, in 2003, and the M.S. and Ph.D. degrees in mechanical engineering from the Nanjing University of Aeronautics and Astronautics (NUAA), Nanjing, China, in 2006 and 2010, respectively. He is currently an Assistant Professor with the College of Mechanical and Electrical Engineering, NUAA. His research interests include design and motion control of bionic mobile robotics and intelligent control systems.

WEI LI received the B.S. degree in mechanical engineering from Beihang University, China, in 2012, and the Ph.D. degree in mechanical engineering from McGill University, Canada, in 2018. He is currently an Assistant Professor with the School of Mechanical Engineering, Shanghai Jiao Tong University. His research interests include robotics, mechanism design, and analysis.